# Large-Signal Simulation of 94 GHz Pulsed Silicon DDR IMPATTs Including the Temperature Transient Effect

*Aritra ACHARYYA [1], Suranjana BANERJEE [2], J. P. BANERJEE [1]*

[1] Institute of Radio Physics and Electronics, University of Calcutta, 92, APC Road, Kolkata-700009, India
[2] Academy of Technology, West Bengal University of Technology, Adisaptagram, Hooghly-712121, West Bengal, India

ari_besu@yahoo.co.in, suranjanarpe21@yahoo.com, jpbanerjee06@rediffmail.com

**Abstract.** *In this paper large-signal modeling and simulation has been carried to study the frequency chirping due to temperature transients and the large-signal power and efficiency of pulsed silicon Double-Drift Region (DDR) Impact Avalanche Transit Time (IMPATT) device operating at 94 GHz. A large-signal simulation method based on non-sinusoidal voltage excitation incorporating the transient thermal effect has been developed by the authors. Results show that the device is capable of delivering a peak pulsed power output of 17.5 W with 12.8% efficiency when the voltage modulation is 60%. The maximum junction temperature rise is 350.2 K for a peak pulsed bias current of 6.79 A with 100 ns pulsewidth and 0.5 percent duty cycle; whereas the chirp bandwidth is 8.3 GHz.*

## Keywords

Chirp bandwidth, frequency chirping, large-signal simulation, pulsed DDR IMPATT, temperature transients.

## 1. Introduction

Impact Avalanche Transit Time (IMPATT) devices are the most efficient solid-state source to deliver significantly high power at millimeter-wave frequencies [1]-[3]. Most of the current research activities for mm-wave systems are concentrated on window frequencies, i.e. 35, 94, 140, 220 GHz where atmospheric attenuation is relatively low. Small-signal analysis and simulation methodologies of IMPATT devices reported so far [4]-[6] provide considerable insight into the high frequency properties of the oscillator. But several important properties of the device such as dependence of RF power output, DC to RF conversion efficiency and frequency tuning on the structural and doping parameters, bias current and RF circuitry cannot be precisely obtained from small-signal analysis. Large-signal modeling and simulation of the device on the other hand can provide accurate information regarding the same. Evans *et al*. [7] in 1968 presented a large-signal model of Read-type (*p*-*n*-*v*-*n*) IMPATT oscillator from which they obtained RF power output and efficiency of the oscillator from a closed-form solution of nonlinear equations. They assumed that the transit time of the charge carriers through the drift region is much shorter than the period of RF oscillation in order to obtain the close-form solution of device equations. Pioneering work on large-signal analysis of Read-type silicon IMPATT oscillator was carried out by Scharfetter *et al.* in 1969 [8]. They presented a self-consistent numerical solution of the device equations describing carrier transport, carrier generation and space-charge balance subject to appropriate boundary conditions and obtained the large-signal admittance and efficiency of silicon Read-type IMPATT diode. Gupta *et al.* [9] in 1973 followed a current-excited method for large-signal analysis of the device with a circuit representation. They assumed a sinusoidal current flowing through the device and obtained the corresponding voltage response to calculate the device impedance. In this paper the authors have developed a large-signal simulation method based on non-sinusoidal voltage excitation [10]-[11] incorporating the transient thermal effect to study the frequency chirping due to temperature transients and the large-signal power and efficiency of pulsed Silicon DDR IMPATT device operating at 94 GHz.

The performance and reliability of IMPATT devices is strongly dependent on the junction temperature of the device and the actual rise of junction temperature in both CW and pulsed mode of operation must be limited to a value much below the burn out temperature. Small-signal simulation method based on Gummel-Blue approach [12] was reported in [13]-[19] to study the millimeter-wave performance of CW DDR Si IMPATT device operating at 94 GHz. In this paper the authors carried out large-signal simulation by using a transient thermal model of the pulsed Si DDR IMPATT device with type-IIA diamond heat sink to study the variation of junction temperature with the pulse-width (50 – 200 ns) and duty cycle (0.25 – 1.0%) of bias current pulse for a fixed repetition rate (50 kHz). The large-signal properties and performance of the device are

found to be very much sensitive to junction temperature under pulsed operation. The peak junction temperature is obtained from the transient thermal analysis [20] by incorporating the temperature dependent material parameters of silicon into the large-signal simulation program. The large-signal power and efficiency of the device are also obtained from this study. RF voltage modulation is varied from 5 to 70% to study the dependence of large-signal power and efficiency of the device. The authors have also studied in this paper the frequency chirping effect due to variation of junction temperature and chirping bandwidth for pulsed operation of the device.

## 2. Large-Signal Modeling and Simulation Technique

One-dimensional model of reverse biased $n^+$-$n$-$p$-$p^+$ structure shown in Fig. 1 is used for the large-signal simulation of DDR IMPATT device since the physical phenomena take place in the semiconductor bulk along the symmetry axis of the mesa structure of IMPATT devices. The fundamental time and space dependent device equations i.e., Poison's equation (1), continuity equations (2), (3) and current density equations (4), (5) involving mobile space charge in the depletion layer are simultaneously solved under large-signal condition with appropriate boundary conditions by using a double-iterative field maximum simulation method. The fundamental device equations are given by:

$$\frac{d\xi(x,t)}{dx} = \frac{q}{\varepsilon_s}\left(N_D - N_A + p(x,t) - n(x,t)\right), \tag{1}$$

$$\frac{\partial p(x,t)}{\partial t} = -\frac{\partial J_p(x,t)}{\partial x} + q\left(n(x,t)\alpha_n(x,t)v_n(x,t) + p(x,t)\alpha_p(x,t)v_p(x,t)\right), \tag{2}$$

$$\frac{\partial n(x,t)}{\partial t} = \frac{\partial J_n(x,t)}{\partial x} + q\left(n(x,t)\alpha_n(x,t)v_n(x,t) + p(x,t)\alpha_p(x,t)v_p(x,t)\right), \tag{3}$$

$$J_p(x,t) = qp(x,t)v_p(x,t) - qD_P\left(\frac{\partial p(x,t)}{\partial x}\right), \tag{4}$$

$$J_n(x,t) = qn(x,t)v_n(x,t) + qD_n\left(\frac{\partial n(x,t)}{\partial x}\right) \tag{5}$$

where $N_D$ and $N_A$ are the donor and acceptor concentrations respectively, $p(x,t)$ and $n(x,t)$ are respectively the electron and hole concentrations at the space point $x$ at the instant $t$, $\xi(x,t)$ is the electric field at $x$ at the instant $t$, $J_n(x,t)$ and $J_p(x,t)$ are respectively the electron and hole components of bias current density ($J_0(t) = J_n(x,t) + J_p(x,t)$) at $x$ at the instant $t$, $q$ is the electric charge of an electron ($q = 1.6\times10^{-19}$ C) and $\varepsilon_s$ is the permittivity of the semiconductor material. In the above mentioned simulation method, the computation starts from the field maximum near the metallurgical junction. Boundary conditions are imposed at the contacts (i.e., $n^+$-$n$ and $p^+$-$p$ interfaces) by setting up appropriate restrictions in equations (1) – (5). The boundary conditions for the electric field at the depletion layer edges are given by:

$$\xi(-x_1,t) = 0 \text{ and } \xi(+x_2,t) = 0\ . \tag{6}$$

Similarly the boundary conditions for normalized current density $P(x,t) = (J_p(x,t) - J_n(x,t)) / J_0(t)$ (where, $J_0(t) = J_p(x,t) + J_n(x,t)$) at the depletion layer edges i.e., at $x = -x_1$ and $x = x_2$ are given by:

$$P(-x_1,t) = \left(\frac{2}{M_p(-x_1,t)} - 1\right) \text{ and } P(+x_2,t) = \left(1 - \frac{2}{M_n(+x_2,t)}\right) \tag{7}$$

where $M_n(x_2,t)$ and $M_p(-x_1,t)$ are the electron and hole multiplication factors at the depletion layer edges are given by:

$$M_p(-x_1,t) = \frac{J_0(t)}{J_p(-x_1,t)} \text{ and } M_n(+x_2,t) = \frac{J_0(t)}{J_n(+x_2,t)}. \tag{8}$$

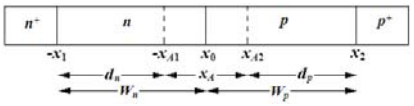


**Fig. 1.** One-dimensional model of DDR IMPATT device.

Time varying diode voltage ($V_B(t)$) and avalanche zone voltage drop ($V_A(t)$) are obtained from numerical integration of the field profile at a particular instant of time $t$ over the depletion layer and avalanche layer widths respectively as follows:

$$V_B(t) = \int_{-x_1}^{x_2} \xi(x,t)dx \text{ and } V_A(t) = \int_{-x_{A1}}^{x_{A2}} \xi(x,t)dx\ . \tag{9}$$

DC values of the peak electric field ($\xi_p$), breakdown voltage ($V_B$) and avalanche zone voltage ($V_A$) drop can be evaluated by taking the time averages of time varying peak electric field ($\xi_p(t)$), breakdown voltage ($V_B(t)$) and avalanche zone voltage ($V_A(t)$) over a complete time period of steady-state oscillation ($T = 1/f$; where $f$ is the fundamental frequency of steady-state oscillation). Thus the DC values of the peak electric field ($\xi_p$), breakdown voltage ($V_B$) and avalanche zone voltage ($V_A$) are given by:

$$\xi_p = \frac{1}{T}\int_0^T \xi_p(t)dt,\ V_B = \frac{1}{T}\int_0^T V_B(t)dt \text{ and } V_A = \frac{1}{T}\int_0^T V_A(t)dt\ . \tag{10}$$

The large-signal simulation is carried out by considering the IMPATT device as a non-sinusoidal voltage driven source, shown in Fig. 2. The input AC voltage is taken as:

$$V_{RF}(t) = V_B\sum_{p=1}^{n} m_x{}^p \sin(p\omega t). \tag{11}$$

The bias voltage is applied through a coupling capacitor ($C$) to study the performance of the device at a given fundamental frequency ($f = \omega/2\pi$) with its $n$ harmonics. The snap-shots of electric field and current density profiles in the depletion layer of IMPATT device are obtained from the simultaneous numerical solution of the basic device equations (1) – (5) subject to appropriate boundary conditions (6), (7). The large-signal simulation is carried out by

taking 500 space steps and 100 - 150 time steps with sufficient accuracy.

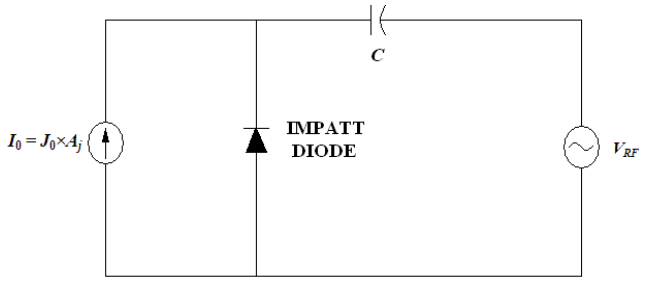


**Fig. 2.** Voltage driven IMPATT diode oscillator and associated circuit.

The large-signal program is run until the limit of one complete cycle (i.e. $0 \le \omega t \le 2\pi$) is reached. A pulsed current source provides the necessary bias current density. The RF voltage amplitude is $V_{RF}$ and operating frequency is $f$. The waveforms associated with terminal current and voltage during a complete cycle of oscillation are Fourier analyzed to study the high frequency characteristics of the device at various instants of time ($\omega t$ = 0, $\pi/2$, $\pi$, $3\pi/2$, $2\pi$). The simulation is repeated at consecutive cycles to confirm the stability of oscillation. The simulated values of large-signal negative conductance ($G(\omega)$), susceptance ($B(\omega)$), negative resistance ($Z_R(\omega)$), reactance ($Z_X(\omega)$) and $Q$-factor ($Q_p = -B_p/G_p$), where $G_p$ and $B_p$ are the large signal peak negative conductance and susceptance at optimum frequency ($f_p$)) respectively are obtained from this study. The large-signal values of negative conductance ($G(\omega)$) and susceptance ($B(\omega)$) (both are normalized by device junction area $A_j$: considering circular cross sectional area of the device, $A_j = \pi(D_j/2)^2$;.where $D_j$ is the device effective junction diameter) are their effective values at the fundamental frequency of the voltage source, obtained by detailed Fourier analysis of the terminal current and voltage waveforms. The large-signal device admittance is $Y_D(\omega) = [G(\omega) + j\, B(\omega)]A_j$. The large-signal device impedance is given by:

$$Z_D(\omega) = \frac{1}{Y_D(\omega)} = \frac{1}{[G(\omega) + jB(\omega)]A_j} = Z_R(\omega) + jZ_X(\omega). \quad (12)$$

The large-signal negative resistance ($Z_R(\omega)$) and reactance ($Z_X(\omega)$) of the device are given by:

$$Z_R(\omega) = \frac{G(\omega)}{[G(\omega)^2 + B(\omega)^2]A_j} \text{ and } Z_X(\omega) = \frac{-B(\omega)}{[G(\omega)^2 + B(\omega)^2]A_j}. \quad (13)$$

The RF power output is calculated from the following expression:

$$P_{RF} = \frac{1}{2} V_{RF}^2 |G_p| A_j \quad (14)$$

where $V_{RF}$ is the RF voltage, $|G_p|$ is the magnitude of peak negative conductance normalized by device effective junction area ($A_j$). The large-signal DC to RF conversion efficiency ($\eta_L$) of IMPATT diode is given by:

$$\eta_L = \frac{P_{RF}}{P_{DC}} \quad (15)$$

where $P_{DC} = J_0 V_B A_j$ is the input DC power and $J_0$ is the amplitude of the pulsed bias current density.

# 3. Results and Discussion

The structural (active layer widths ($W_n$, $W_p$)) and doping ($n$- and $p$-layer doping concentrations ($N_D$, $N_A$), $n^+$- and $p^+$-layer doping concentrations ($N_{n+}$, $N_{p+}$)) of the device and amplitude of pulsed bias current density ($J_0$) are varied to optimize the large-signal power and efficiency. The optimized doping and structural parameters as well as the magnitude of peak pulsed bias current density ($J_0$) are given in Tab. 1. The realistic field and temperature dependent ionization rates ($\alpha_n$, $\alpha_p$) and drift velocities ($v_n$, $v_p$) of Si and other material parameters such as bandgap ($E_g$), intrinsic carrier concentration ($n_i$), effective density of states of conduction and valance bands ($N_c$, $N_v$), diffusion coefficients ($D_n$, $D_p$), mobilities ($\mu_n$, $\mu_p$), diffusion lengths ($L_n$, $L_p$) of charge carriers and permittivity ($\varepsilon_s$) are taken from published experimental data [21]-[24].

| $J_0$ ($\times 10^8$ A m$^{-2}$) | $W_n$ (μm) | $W_p$ (μm) | $N_D$ ($\times 10^{23}$ m$^{-3}$) | $N_A$ ($\times 10^{23}$ m$^{-3}$) | $N_{n+}$, $N_{p+}$ ($\times 10^{26}$ m$^{-3}$) |
|---|---|---|---|---|---|
| 6.00 | 0.435 | 0.415 | 1.100 | 1.150 | 1.000 |

**Tab. 1.** Design parameters.

## 3.1 Static Properties

The important static parameters of the device such as peak electric field ($\xi_p$), breakdown voltage ($V_B$), avalanche voltage ($V_A$), ratio of drift layer voltage to breakdown voltage ($V_D/V_B$), avalanche layer width ($x_A$), ratio of avalanche layer width to total drift layer width ($x_A/W$) of pulsed DDR Si IMPATT device designed at 94 GHz are obtained from the output of DC simulation program at different junction temperatures ($T_j$) for $m_x = 0$. These parameters are given in Tab. 2. The variations of peak electric field ($\xi_p$), breakdown voltage ($V_B$), avalanche voltage ($V_A$) with junction temperature ($T_j$) are shown in Fig. 3. It is observed from Fig. 3 that the $\xi_p$, $V_B$, and $V_A$ increase with the junction temperature ($T_j$). The increase of breakdown voltage with junction temperature is more appreciable than that of avalanche voltage. Thus with the increase of junction temperature ($T_j$) the ratio of drift zone voltage to breakdown voltage ($V_D/V_B$; where $V_D = V_B - V_A$) remains almost constant. The ratio $V_D/V_B$ attains a maximum value of 32.53% at a junction temperature of 500 K. Tab. 2 shows that the avalanche zone width ($x_A$) expands from 0.300 to 0.350 μm and the ratio of avalanche zone to depletion layer width ($x_A/W$; where $W = W_n + W_p$) increases from 35.29% to 41.88% as the junction temperature ($T_j$) rises from 300 K to 500 K.

| DC PARAMETERS | JUNCTION TEMPERATURE ($T_j$) | | | | |
|---|---|---|---|---|---|
| | 300 K | 350 K | 400 K | 450 K | 500 K |
| $\xi_p$ ($\times 10^7$ V m$^{-1}$) | 5.2868 | 5.4618 | 5.6368 | 5.8118 | 5.9868 |
| $V_B$ (V) | 18.22 | 19.64 | 21.13 | 22.68 | 24.31 |
| $V_A$ (V) | 12.29 | 13.31 | 14.26 | 15.37 | 16.40 |
| $V_D / V_B$ (%) | 32.51 | 32.26 | 32.49 | 32.26 | 32.53 |
| $x_A$ (μm) | 0.300 | 0.314 | 0.328 | 0.344 | 0.356 |
| $x_A/W$ (%) | 35.29 | 36.94 | 38.58 | 40.47 | 41.88 |

**Tab. 2.** Static parameters.

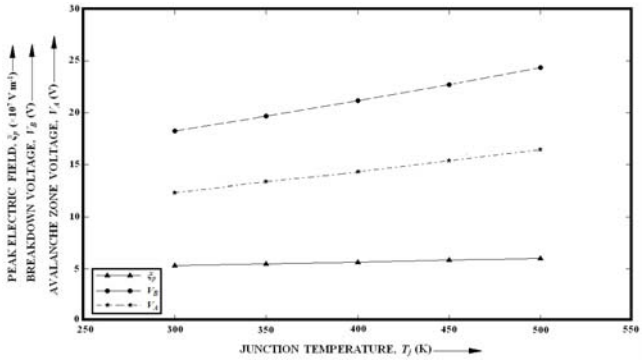


**Fig. 3.** Variations of peak electric field, breakdown voltage and avalanche zone voltage with junction temperature.

## 3.2 Large-Signal Properties

Fig. 4 shows the diode voltage ($V_B(t)$) and particle current ($I_0(t) = J_0(t) \times A_j$) waveforms at 350 K for two consecutive cycles of steady-state oscillation taking 60% voltage modulation. Both the waveforms are observed to be non-sinusoidal. The average values of diode voltage and particle current are found to be 19.64 V and 6.79 A respectively. Further it is observed from Fig. 4 that the phase shift between the diode voltage and particle current is nearly $180^0$, an essential condition for realizing maximum negative resistance and power from the device.

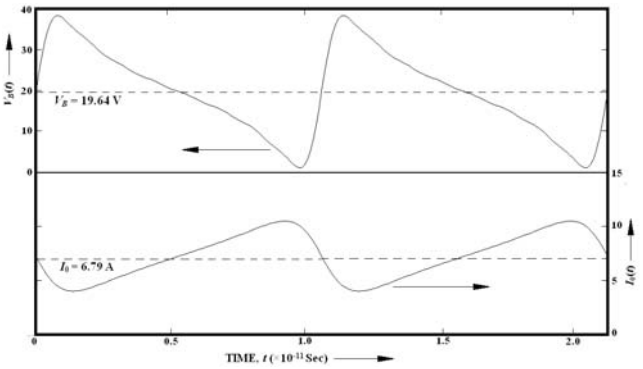


**Fig. 4.** Diode voltage and particle current waveforms at 350 K for two consecutive cycles of steady-state oscillation taking 60% voltage modulation.

The large signal snap-shots of electric field at quarter cycle intervals of steady-state oscillation are shown in Fig. 5 (a) through (e) for 60% voltage modulation and at different junction temperatures. The magnitude of peak field at the junction attains a maximum value when the phase angle is $\omega t = \pi/2$ and $T_j$ is 500 K as seen from Fig. 5 (b). It is interesting to observe that the magnitude of peak field decreases with the decrease of junction temperature (Fig. 5 (a) – (e)). Fig. 5 (b) shows appreciable field distortion in the electron drift layer (*n*-side) as compared to that in the hole drift layer (*p*-side). This may be explained from the fact that electrons have higher ionization rate than holes in silicon for the entire field range of interest. The higher ionization rate of electrons leads to increased generation of electrons compared to that of holes and therefore the mobile carrier (electron) density is higher on *n*-side than that (hole) density on *p*-side. It is reported in [25]-[26] that when mobile charge density increases to a very high value approaching the immobile charge density [25]-[26], the nonlinear distortion of electric field occurs. The electric field snap-shot shows more nonlinearity and distortion at higher temperature i.e. 500 K than at lower temperature i.e. 300 K as seen from Fig. 5 (b). The electric field being lower at lower junction temperatures, the ionization rate is also lower and so the electron generation rate is lower on the *n*-side. Under this situation mobile carrier density at lower junction temperature is not high enough to cause the distortion in the electric field profile.

Electric field snap-shots show depletion width modulation at large-signal level as shown in Fig. 5 (a) to (e). This modulation changes at different phase angles as well as at different junction temperatures. Also the depletion width modulation is different for electron and hole drift layers. Higher depletion width modulation suggests higher punch through factor. Maximum modulation occurs at the phase angle of $\omega t = \pi/2$ at all junction temperatures under consideration. Also the depletion width modulation increases with the increase of junction temperature at all phase angles ($\omega t = 0, \pi/2, \pi, 3\pi/2, 2\pi$).

Variations of peak negative conductance ($G_p$) and susceptance ($B_p$) with RF voltage are shown in Fig. 6 at different junction temperatures by considering the voltage modulation factor ($m_x$) in the range of 5 to 70%. The magni

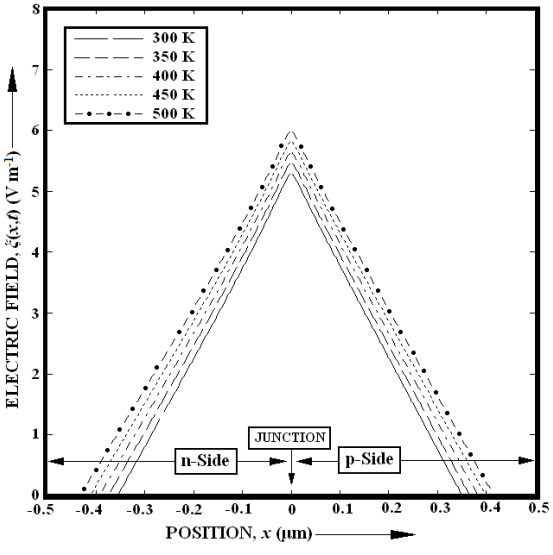


**(a)** $\omega t = 0$

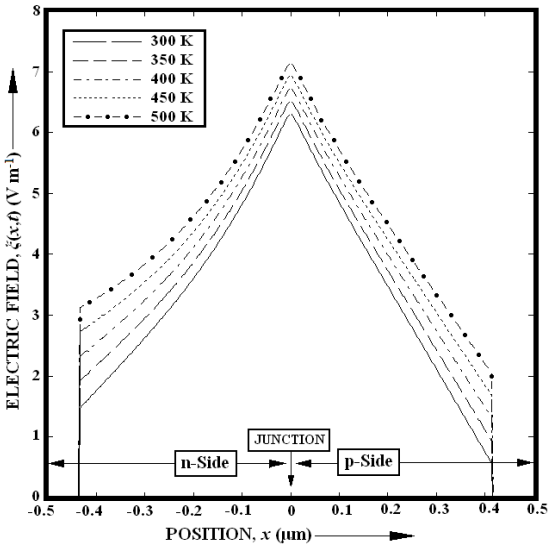


**(b)** $\omega t = \pi/2$

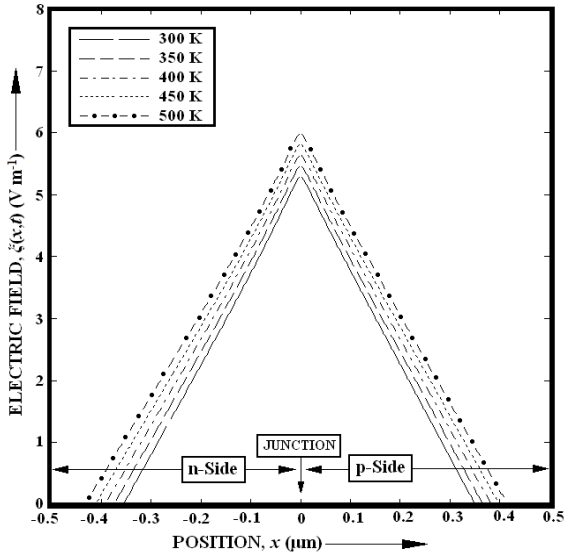


**(c)** $\omega t = \pi$

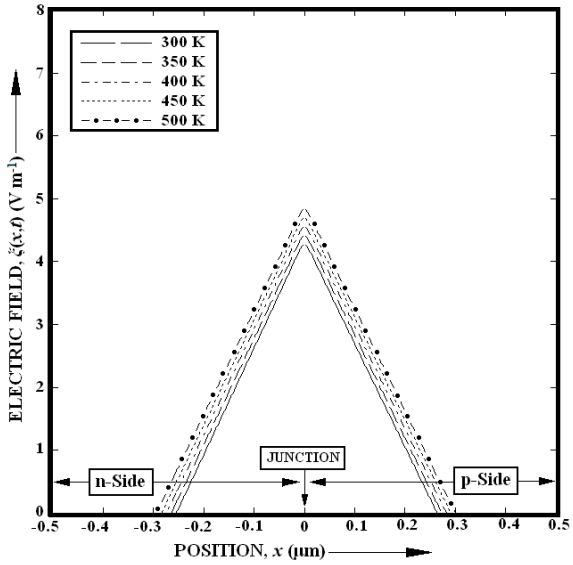


**(d)** $\omega t = 3\pi/2$

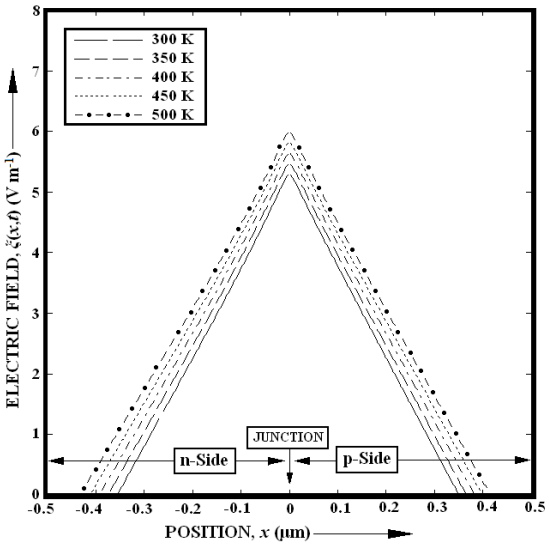


**(e)** $\omega t = 2\pi$

**Fig. 5.** Large signal electric field snap-shots at each quarter cycle of steady-state oscillation (a) ω = 0, (b) ω = π/2, (c) ω = π, (d) ω = 3π/2 and (e) ω = 2π for different junction temperatures (voltage modulation is 60%).

tude of $G_p$ ($|G_p|$) decreases with the increase of RF voltage at a particular junction temperature. It also decreases with the increase of junction temperature at a particular voltage modulation factor ($m_x$). The magnitude of $|B_p|$ also decreases with the increase of RF voltage at a particular junction temperature and with the increase of junction temperature at a particular voltage modulation factor ($m_x$). Fig. 7 shows the variations of optimum frequency ($f_p$) for peak negative conductance ($G_p$), peak pulsed power output ($P_{RF}$) and large-signal DC to RF conversion efficiency ($\eta_L$) with RF voltage at different junction temperatures. The optimum frequency ($f_p$) of the device decreases with the increase of RF voltage at a particular junction temperature. The variations of peak pulsed power output ($P_{RF}$) and large-signal DC to RF conversion efficiency ($\eta_L$) with RF voltage at different junction temperatures are shown in Fig. 7. The junction area of the device ($A_j$) for pulsed operation is taken to be $1.131\times10^{-8}$ m$^{-2}$ by considering a circular cross-section of the device with junction diameter ($D_j$) of 120 μm [27]. It is interesting to observe from Fig. 7 that the RF power output increases sharply with the increase of voltage modulation ($m_x$) upto 60%, after which it decreases slowly. When the voltage modulation exceeds 65% the RF power output falls sharply with the increase of voltage modulation factor. This sharp fall of RF power output is due to sharp decrease in the magnitude of $G_p$ for voltage modulation exceeding 65%. The variation of large-signal efficiency with RF voltage follows a similar nature as that of $P_{RF}$. The simulation results clearly indicate that the voltage modulation should be kept below 65% to realize optimum performance from pulsed DDR Si IMPATTs as regards high power with high conversion efficiency.

The large-signal admittance characteristics of the device are obtained at different junction temperatures for a voltage modulation of 60% and plotted in Fig. 8. The op-

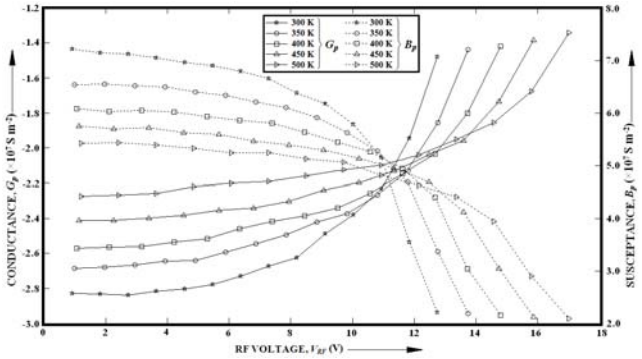


**Fig. 6.** Variations of peak negative conductance and peak susceptance with RF voltage at different junction temperatures.

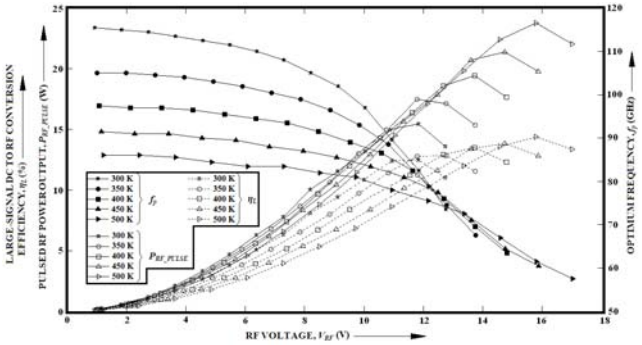


**Fig. 7.** Variations of peak optimum frequency, large-signal DC to RF conversion efficiency and pulsed power output with RF voltage at different junction temperatures.

timum frequency ($f_p$) for peak negative conductance decreases from 102.5 to 76 GHz when the junction temperature increases from 300 to 500 K. The optimum frequency is exactly equal to the design window frequency at a junction temperature of 350 K. The $Q$-factor of the device decreases slightly from 2.31 to 2.12 when the junction temperature increases from 300 to 500 K. The $Q$-factor corresponding to the peak junction temperature of 350.2 K, determined from transient thermal analysis is found to be 2.20. The lower the value of $Q$-factor being close to unity, the better is the device performance.

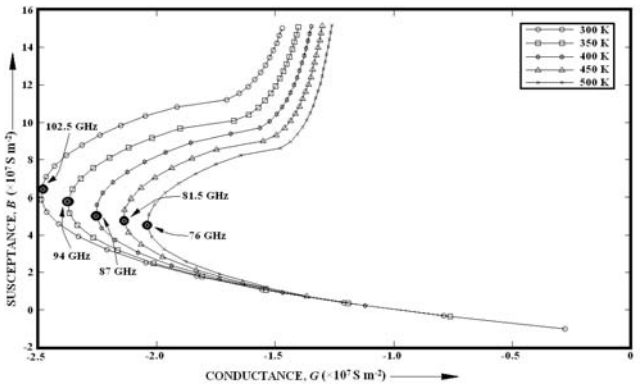


**Fig. 8.** Admittance characteristics (10 – 200 GHz) of pulsed DDR Si IMPATTs at different junction temperatures (taking 60% voltage modulation).

## 3.3 Results of Transient Thermal Analysis and Frequency Chirping

Type-IIA diamond heat sink having diameter ($D_H$) of 5.0 mm and thickness ($L_H$) of 2.0 mm is considered for the transient thermal analysis of 94 GHz pulsed Si DDR IMPATT device. Step function is used to represent the input bias current pulse (pulsewidths, $T_{on}$ = 50, 100, 150 and 200 ns, duty cycle, $d$ = 0.25, 0.50, 0.75, 1.00% and repetition rate, $f_{Pulse}$ = 50 kHz). The pulsed bias current density may be expressed as:

$$J_{Pulse}(t) = J_0 \sum_{i=0}^{\infty} \left[ u(t - iT) - u(t - iT - T_{on}) \right] \tag{16}$$

where $J_0$ is the optimum amplitude of the pulsed bias current density. The unit step function is defined as:

$$\left.\begin{aligned} u(t-T) &= 1 \quad \text{for} \quad t \geq T \\ u(t-T) &= 0 \quad \text{for} \quad t < T \end{aligned}\right\} \tag{17}$$

The program for transient thermal model developed by the authors is used to compute the junction temperature transients for different bias current pulsewidths with a fixed repetition rate. Fig. 9 shows the junction temperature transients of the device mounted on type-IIA diamond heat sink. It is observed from Fig. 9 that, the junction temperature of the device gradually increases from the ambient temperature ($T_a$ = 300 K) during the on-time of the applied current pulse and reaches the maximum temperature at the end of the on time ($T_{max}$ = 350.2 K at $T_{on}$ = 100 ns). Again the junction temperature decays gradually during the off-period of the applied current pulse ($t > T_{on}$) and falls to ambient temperature before completion of the full cycle ($t = T_{Pulse} = T_{on} + T_{off}$ = 20 μs). As expected the peak optimum frequency changes due to temperature transient during on-time and off-time of the bias current pulse. This is known as frequency chirping effect due to variation of junction temperature.

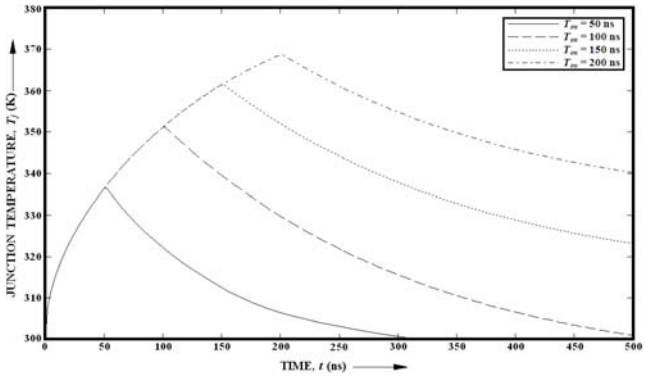


**Fig. 9.** Temperature transients for 60% voltage modulation.

Fig. 10 shows the time variation of $f_p(T_j)$ of 94 GHz pulsed Si DDR IMPATT with semi-infinite type-IIA diamond heat sink. Fig. 11 shows the variations of chirp bandwidth ($BW_c = f_p(T_a) - f_p(T_{max})$) with pulsewidth. The

chirp bandwidth ($BW_c$) increases almost linearly with the bias current pulsewidth. Usually the W-band (75 – 110 GHz) pulsed Si DDR IMPATTs are operated with bias current pulse of 100 ns pulsewidth and 0.5% duty cycle [27]-[28]. The thermal analysis presented in this paper shows that the maximum junction temperature rise is 350.2 K for a peak pulsed bias current of 6.79 A with 100 ns pulsewidth and 0.5% duty cycle; whereas the chirp bandwidth is 8.3 GHz. After repetitive run of large-signal program with transient thermal model, the peak value of junction temperature at the end of the on time ($T_{on}$ = 100 ns) of the applied bias current pulse is found to be 350.2 K.

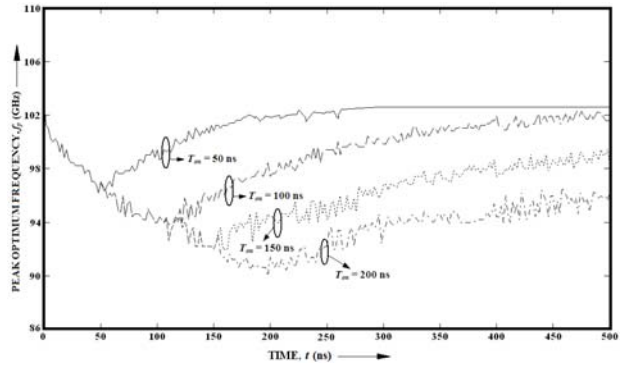


**Fig. 10.** Time variation of peak optimum frequency for 60% voltage modulation.

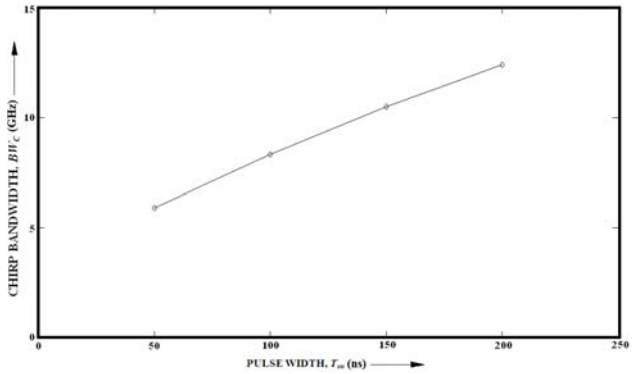


**Fig. 11.** Variation of chirping bandwidth with pulsewidth.

### 3.4 Comparison with Experimental Results

Chang *et al*. [27] in 1979 fabricated 94 GHz DDR Si IMPATT diode and measured the power output by biasing the diode with pulsed current of 100 ns pulsewidth and 0.5% duty cycle. They obtained a peak pulsed power of 13 to 15 W from the IMPATT source. The large-signal simulation of 94 GHz DDR Si IMPATT presented in this paper shows that the device delivers a power of 17.5 W with 12.8% DC to RF conversion efficiency at 60% voltage modulation when it is driven by a pulsed bias current of 6.79 A with 100 ns pulse width, 0.5% duty cycle and 50 kHz repetition rate. So the large signal simulation results presented in this paper are in close agreement with the experimental report by Chang *et al*. [27].

## 4. Conclusion

In this paper the large-signal properties of 94 GHz pulsed Si DDR IMPATT device due to temperature transient effect and consequent frequency chirping phenomenon has been studied. A transient thermal model and a large-signal simulation method based on non-sinusoidal voltage excitation have been developed by the authors to study the effect temperature transients on the large-signal characteristics and frequency chirping in pulsed Si DDR IMPATTs. The simulation results presented in this paper show that the device can deliver a peak pulsed power output of 17.5 W with 12.8% DC to RF conversion efficiency which are in close agreement with experimental reports for pulsed Si DDR IMPATT source.

## References

[1] MIDFORD, T. A., BERNICK, R. L. Millimeter wave CW IMPATT diodes and oscillators. *IEEE Trans. Microwave Theory Tech.*, 1979, vol. 27, p. 483-492.

[2] CHANG, Y., HELLUM, J. M., PAUL, J. A., WELLER, K. P. Millimeter-wave IMPATT sources for communication applications. *IEEE MTT-S International Microwave Symposium Digest*, 1977, p. 216-219.

[3] GRAY, W. W., KIKUSHIMA, L., MORENTC, N. P., WAGNER, R. J. Applying IMPATT power sources to modern microwave systems. *IEEE Journal of Solid-State Circuits*, 1969, vol. 4, p. 409 to 413.

[4] MISWA, T. Negative resistance in p-n junctions under avalanche breakdown conditions. *IEEE Trans Electron Devices*, 1966, vol. ED-33, p. 137- 151.

[5] GILDEN, M., HINES, M. E. Electronic tuning effects in the Read microwave avalanche diode. *IEEE Trans. on Electron Devices*, 1966, vol. ED-13, no. 1, pp. 169-175.

[6] GUMMEL, H. K., SCHARFETTER, D. L. Avalanche region of IMPATT diodes. *Bell Sys. Tech. J.*, 1966, vol. 45, p. 1797-1828.

[7] EVANS, W. J., HADDAD, G. I. A large-signal analysis of IMPATT diodes. *IEEE Trans. on Electron Devices*, 1968, vol. ED-15, no. 10, p. 708-717.

[8] SCHARFETTER, D. L., GUMMEL, H. K. Large-signal analysis of a silicon Read diode oscillator. *IEEE Trans. on Electron Devices*, 1969, vol. ED-16, no. 1, p. 64-77.

[9] GUPTA, M. S., LOMAX, R. J. A Current-excited large-signal analysis of IMPATT devices and its circuit implementations. *IEEE Trans. on Electron Devices*, 1973, vol. ED-20, p. 395-399.

[10] ACHARYYA, A., BANERJEE, S., BANERJEE, J. P. Effect of junction temperature on the large-signal properties of a 94 GHz silicon based double-drift region impact avalanche transit time device. *Journal of Semiconductors*, Accepted, 2013, vol. 34, issue 1.

[11] ACHARYYA, A., BANERJEE, S., BANERJEE, J. P. A proposed method to study the parasitic resistance of Ka-band silicon IMPATT diode from large-signal electric field snap-shots. In *International Conf. on Communications, Devices and Intelligent Systems (CODIS) 2012.* Jadavpur University, W. B., India, Accepted, 2012.

[12] GUMMEL, H. K., BLUE, J. L. A small-signal theory of avalanche noise in IMPATT diodes. *IEEE Trans. on Electron Devices*, 1967, vol. 14, no. 9, p. 569-580.

[13] ACHARYYA, A., BANERJEE, J. P. Dependence of avalanche response time on photon flux incident on DDR silicon IMPATT devices. In *Progress In Electromagnetics Research Symposium Proceedings*. Moscow (Russia), August 19-23, 2012, p. 867-872.

[14] ACHARYYA, A., BANERJEE, J. P. Potentiality of IMPATT devices as terahertz source: An avalanche response time based approach to determine the upper cut-off frequency limits. *IETE Journal of Research*. Accepted, publication schedule: March-April 2013.

[15] ACHARYYA, A., BANERJEE, J. P. Analysis of photo-irradiated double-drift region silicon impact avalanche transit time devices in the millimeter-wave and terahertz regime. *Terahertz Science and Technology*, 2012, vol. 5, no. 2, p. 97-113.

[16] ACHARYYA, A., BANERJEE, S., BANERJEE, J. P. Calculation of avalanche response time for determining the high frequency performance limitations of IMPATT devices. *Journal of Electron Devices*, 2012, vol. 12, p. 756-760.

[17] ACHARYYA, A., BANERJEE, S., BANERJEE, J. P. Dependence of DC and small-signal properties of double drift region silicon IMPATT device on junction temperature. *Journal of Electron Devices*, 2012, vol. 12, p. 725-729.

[18] ROY, S. K., SRIDHARAN, M., GHOSH, R., PAL, B. B. Computer methods for the dc field and carrier current profiles in IMPATT devices starting from the field extremum in the depletion layer. In *Proc. of NASECODE-I Conf. on Numerical Analysis of Semiconductor Devices.* Dublin: Boole Press, 1979, p. 266-274.

[19] ROY, S. K., BANERJEE, J. P., PATI, S. P. A computer analysis of the distribution of high frequency negative resistance in the depletion layers of IMPATT diodes. In *Proc. of NASECODE-IV Conf. on Numerical Analysis of Semiconductor Devices.* Dublin: Boole Press, 1985, p. 494-500.

[20] OLSON, H. M. Temperature transients in IMPATT diodes. *IEEE Trans. on Electron Devices*, 1976, vol. ED-23, no. 5, p. 494-503.

[21] GRANT, W. N. Electron and hole ionization rates in epitaxial silicon. *Solid State Electron*, 1973, vol. 16, no. 10, p. 1189-1203.

[22] CANALI, C., OTTAVIANI, G., QUARANTA, A. A. Drift velocity of electrons and holes and associated anisotropic effects in silicon. *J. Phys. Chem. Solids*, 1971, vol. 32, no. 8, p. 1707.

[23] ZEGHBROECK, B.V. *Principles of Semiconductor Devices*, Colorado Press, 2011.

[24] "Electronic Archive: New Semiconductor Materials, Characteristics and Properties," http://www.ioffe.ru/SVA/NSM/Semicond/Si/index.html.

[25] SRIDHARAN, M., ROY, S. K. Computer studies on the widening of the avalanche zone and decrease on efficiency in silicon X-band symmetrical DDR. *Electron Lett.*, 1978, vol. 14, p. 635-637.

[26] SRIDHARAN, M., ROY, S. K. Effect of mobile space charge on the small signal admittance of silicon DDR. *Solid State Electron*, 1980, vol. 23, p. 1001-1003.

[27] CHANG, K., SUN, C., ENGLISH, D. L., NAKAII, E. M., High power 94-GHz pulsed IMPATT oscillators. In *IEEE MTT-S International Microwave Symposium Digest*, 1979, p. 71-72.

[28] FONG, T. T., KUNO, H. J. Millimeter-wave pulsed IMPATT sources. *IEEE Trans. Microwave Theory Tech.*, 1979, vol. 27, no. 5, p. 492-499.

## About Authors ...

**Aritra ACHARYYA** received his M.Tech. degree from Institute of Radio Physics and Electronics, University of Calcutta, Kolkata, W.B., India. Earlier he obtained his B.E. Degree from Bengal Engineering and Science University, Shibpur, Howrah, W.B., India. He is the recipient of Pareshlal Dhar Bhowmik book award in the year 2010 for securing highest marks in M. Tech. (Radio Physics and Electronics) Examination 2010 of University of Calcutta. His research interest is Millimeter-wave and Terahertz Semiconductor Devices more specifically IMPATT Devices. He is the principle co-author of more than 35 research papers in different national and international journals and conference proceedings.

**Suranjana BANERJEE** received her M.Tech. degree from Institute of Radio Physics and Electronics, University of Calcutta, Kolkata, W.B., India. Presently she has been working as Assistant Professor in the Academy of Technology, West Bengal University of Technology, Adisaptagram, Hooghly 712121, West Bengal, India.

**Professor (Dr.) J. P. BANERJEE** obtained B.Sc. (Hons.) and M.Sc. in Physics and Ph.D. in Radio Physics and Electronics from University of Calcutta. He joined the Department of Electronic Science, C.U. in 1989 as a Reader. He has been working as a Professor in the Institute of Radio Physics and Electronics, C.U. since 1998. He is the recipient of Indian National Science Academy Award of a visiting fellowship and Griffith Memorial Prize in Science of the Calcutta University in 1986. He is the principle co-author of more than 150 research papers in International Journals in the fields of Semiconductor Science and Technology, Microwave and Millimeter-wave Avalanche Transit Time Devices and Avalanche Photo Detectors.